January 2020

Effect Of Wind Direction On Sea Surface Reflectance

Seyedmojtaba Shahabi

EFFECT OF WIND DIRECTION ON SEA SURFACE REFLECTANCE

by

Seyedmojtaba Shahabi

Master of Science, University of North Dakota, 2020

A Thesis

Submitted to the Graduate Faculty of the

University of North Dakota

In partial fulfillment of the requirements for the degree of

Master of Science

Grand Forks, North Dakota

August 2020

Name: Seyedmojtaba Shahabi

Degree: Master of Science

        This document, submitted in partial fulfillment of the requirements for the degree from the University of North Dakota, has been read by the Faculty Advisory Committee under whom the work has been done and is hereby approved.

Xiaodong Zhang

Jeffrey VanLooy

Sean Hammond

        This document is being submitted by the appointed advisory committee as having met all the requirements of the School of Graduate Studies at the University of North Dakota and is hereby approved.

Chris Nelson
Dean of the School of Graduate Studies

8/7/2020

Date

PERMISSION

Title   EFFECT OF WIND DIRECTION ON SEA SURFACE REFLECTANCE

Department   Earth System Sciences and Policy

Degree   Master of Science

In presenting this thesis in partial fulfillment of the requirements for a graduate degree from the University of North Dakota, I agree that the library of this University shall make it freely available for inspection. I further agree that permission for extensive copying for scholarly purposes may be granted by the professor who supervised my thesis work or, in his absence, by the Chairperson of the department or the dean of the School of Graduate Studies. It is understood that any copying or publication or other use of this thesis or part thereof for financial gain shall not be allowed without my written permission. It is also understood that due recognition shall be given to me and to the University of North Dakota in any scholarly use which may be made of any material in my thesis.

Seyedmojtaba Shahabi

Date: *08/03/2020*

Acknowledgment

First and foremost, I express my deepest gratitude to my advisor, Prof. Zhang. I thank him for his patience, enormous support, continual encouragement, and mentorship that has guided me through my research. I also wish to thank him for allowing me to work on this project and allowing me to grow professionally and develop my skills in this field. I cannot possibly express my gratitude in enough words to thank him for everything he has done for me. As well, I would like to show my appreciation to all other advisory committee members: Prof. VanLooy for his encouragement and valuable advice with regards to my research and life. I would like to thank Prof. Hammond for his patient guidance, enthusiastic encouragement, and useful critiques of this research work. I also appreciate Earth System Science and Policy department chair Prof. Laguette for being always open and supportive to me. Last but not least, I would also like to thank Shuangyan He for her contribution to this project and assistance. Moreover, I would like to thank the ESSP program to give me this opportunity. Last, but not least, I take this opportunity to give special thanks to my family and friends, especially my parents and my wife for their sacrifices, patience, and support.

Table of Contents

List of Figures

List of Tables

Abstract

The slope distribution of the sea surface varies with the speed as well as the direction of the wind. However, the dependence on wind direction is frequently ignored in the studies of the sea surface reflectance. In this study, we investigate the effect of wind directions on the sea surface reflectance (ρ_s).

Zhang et al. 2017 sea surface reflectance model is followed where the sea surface in our study is modeled using the Cox and Munk (1954) anisotropic model. The Cox and Munk model has an inherent uncertainty relating to the distribution of capillary wave facets and wind speeds, which affects the estimate of surface reflectance. This leads to an inherent uncertainty in estimating surface reflectance of 5-20%, depending on the Sun-viewing geometry and wind speeds.

For a typical setup of sensors measuring the sea surface reflectance, where sensor viewing angle(θ_{sensor}) = 40° and sensor azimuth angle (φ_{sensor}) = 45° to 90° relative to the Sun direction, we found the wind direction would either enhance or diminish Sun glint by up to a factor of 10, whereas its effect on skylight glint is less than 5%. The effect on total sea surface reflectance, including both Sun and skylight glints, therefore depends on the relative importance of Sun glint and the exact direction of the wind. In general, the effect of wind directions is less than the inherent uncertainty of the Cox and Munk model and hence can be ignored when Sun zenith angle (θ_{Sun}) is greater than 40°. When θ_{Sun} < 40°, the effect varies with the exact Sun-viewing geometry and the wind direction. In particular, when θ_{Sun} < 20°

and wind speed > 7.5 m s^{-1}, the maximum effect of ignoring the wind direction could reach up to 35%.

Chapter I

Introduction

The oceans cover about 70% of the earth's surface; the life of the oceans plays a critical role in the life of the whole planet and the planet's climate [1]. The optical properties of natural waters are directly connected to the different kinds of organic and inorganic particles in the water [2, 3]. Remote sensing of the oceans is a key technology for monitoring natural resources change and understanding the global heat and carbon exchange and as a result the climate change impacts. For example, the variation and concentration of phytoplankton as the main source of the food for marine and investigating the algae blooms which have negative impacts in coastal areas are the main purposes of the remote sensing of the oceans [1, 3]

The optical properties of water can be categorized into two groups, inherent optical properties and apparent optical properties. Inherent optical properties of water only depend on the water body and are independent of the interaction between light field and water; IOPs include the volume scattering function, refraction index, and absorption coefficient [2]. Apparent optical properties of water depend not only on the water body but on the geometry of the light and sensor, environments, properties of the light source, etc. such as irradiance reflectance and water-leaving radiance [2].

Most of the sunlight that reaches the water surface passes the water surface and is transmitted to the water body. However, the water surface reflects some of the light back to the air [2]. Water-leaving radiance (L_w) is the main quantity of ocean color measurements which is the transferred upwelling radiance across the water and air body and measured just above the water [4]. Underwater radiometry and above water radiometry are two major methods to measure this quantity. Underwater radiometry is done in fixed depths or a vertical depth profile. However, above water radiometry is done from a platform far from the water surface or just an above water surface radiometer with a blocked skylight [4].

Underwater radiometry is usually done by floating structure to estimate the nadir water-leaving radiance, L_{wn}, which is calculated by measured nadir upwelling radiances at different water depths ($L_{u\,(z)}$ where u stands for upwelling and z is depths) (Fig. 1) and assuming $L_{u\,(z)}$ varies with depth exponentially with a constant diffuse attenuation coefficient (K_{Lu}) [5, 6].
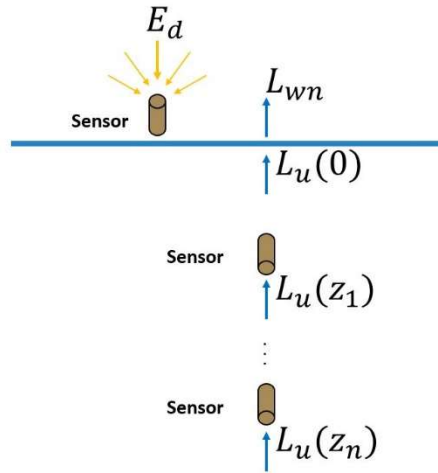
Figure 1. Schematic of underwater radiometry. E_d is nadir downwelling irradiance, L_{wn} is nadir water-leaving radiance, and $L_u\,(z)$ is nadir upwelling radiances at water depth (z).

Underwater radiometry is the essential field measurement method to determine the apparent optical properties of water [7] with a vertical resolution from depth (0) to depths (z) [4]. However, this method deals with some difficulties and uncertainties. The main source of

uncertainty for underwater radiometry is the choice of depths of measurements. For example, depth Z_1 is specified by a shallow depth to minimize the propagation of light from depth Z_1 to 0. However, choosing a very shallow depth would increase the chance of non-vertical measurements due to the waves or the measurement broaching the water surface [4]. The depth from Z_2 to Z_1 should be chosen to minimize the uncertainties in estimated K_{Lu}. However, there are always limitations to the length of the structure [4]. The ocean waves and tilted platform or sensors cause the radiometers subject to non-vertical measurements or depth uncertainty which need to be filtered [4, 6]. Such platforms and sensors are subjected to bio-fouling resulted from algae which need occasional cleaning or using specific materials [4]. Additionally, underwater radiometry deals with self-shadowing or self-reflecting by the platform or other components. However, some studies have suggested self-shadowing corrections [8-10].

In the above-water radiometry, there are sensors set up above the water to measure the radiance (L_t) at a proper angle (θ) and sky radiance at the specular direction (L'_s) which is reflected into the sensor at the water surface (L_r) (Fig. 2).
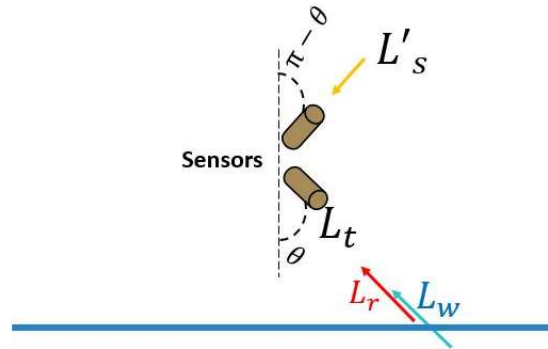
Figure 2. Schematic of above water radiometry. L_t is measured radiance by the sensor, L_r and L_w are reflected skylight and water-leaving radiance respectively. L'_s is the skylight that would be reflected in the sensor by a flat sea surface.

Above-water radiometry deals with difficulties and uncertainties as well [4]. Tilt and rotation of the platform which need to be measured and observations should be corrected.

However, for sensors on fixed platforms tilt and rotation is not an issue [4]. In general, the sensor azimuth angle of 90°-135° away from the sun direction and viewing angle ~ 40° have been suggested to minimize the impact of direct sun glint [4, 11]. Above water radiometry deals with self-shadowing or self-reflecting by the platform as well; where the boat or any object contributes to the light in the hemisphere view of the sensor which measures the downwelling irradiance (E_d) [4]. The most important difficulty of above water radiometry is removing the sunlight and skylight in which the roughness of the water surface and its variation with wind speed and wind direction affects the measurements [2, 4]. The just above water surface radiometry with a blocked skylight method has been proposed to block the glints using a cone in the above-water radiance measurement setup (Fig. 3) [12, 13]. However, this method which has its issue of self-shading, tilted platform, and bio-fouling has not been widely adopted [4]. Also, many observational infrastructures for measuring water-leaving radiance have already been installed [14]. The most dominant above water radiometry is done by spaceborne sensors due to the large spatial coverage and their temporal resolution. However, they also deal with atmospheric correction. Additionally, space-borne sensors are developed for a specific mission, and therefore, after lunch, it is impossible to modify the spatial or spectral resolution of the sensors.
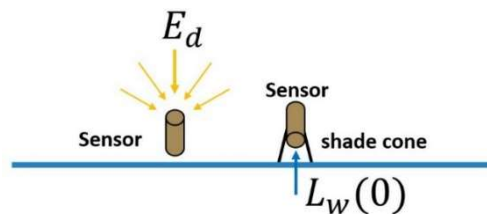
Figure 3. Schematic of just above water surface radiometry with a shade cone. E_d is nadir downwelling irradiance and $L_w(0)$ is nadir water-leaving radiance just above the water.

The roughness of the water surface and its variation with wind causes an above-water radiometer, which is designed to measure water-leaving radiance, unavoidably measures

surface-reflected light coming from the sky and the sun (glints) (Fig.4) [15]. Therefore, these directly reflected skylights (or sky glint) and reflected sunlight (or sun glint) must be subtracted from measured radiance to derive the water-leaving radiance (Eq. (1)).

(a)   (b)
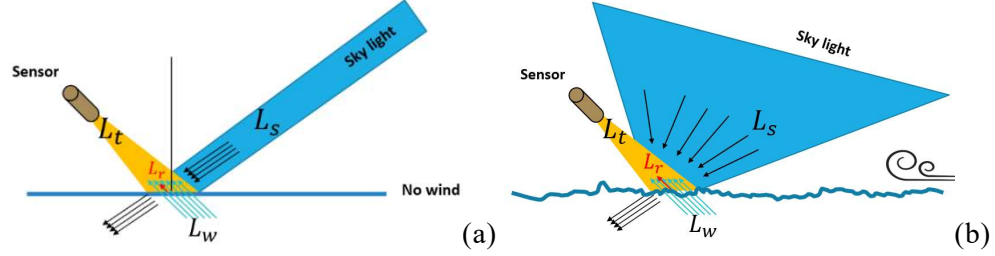
Figure 4. Skylight reflectance by the water surface. (a) no wind, (b) wind speed $\neq 0$ where there are quite small water facets which are inclined to reflect an incoming ray from other portions of the sky towards the sensor. L_t is measured radiance by the sensor's field of view, L_w is the water-leaving radiance, L_s is the skylight, and L_r is the skylight reflected into the sensor's FOV by the water surface.

$$L_t = L_w + L_r. \tag{1}$$

In Eq. (1), L_t is the measured radiance by the sensor's field of view (FOV), L_w is the water-leaving radiance, and L_r is the skylight reflected into the sensor's FOV by the water surface. The skylight reflected by a roughed sea surface into an arbitrary direction Ω, $L_r(\Omega)$, can be calculated by an integral over the entire skydome:

$$L_r(\Omega) = \int_{2\pi} p(\Omega' \to \Omega) \times r(\Omega' \to \Omega) \times L_s(\Omega') \times d\Omega', \tag{2}$$

where $p(\Omega \to \Omega')$ is the probability of capillary wave facets with an orientation that would mirror-reflect the skylight (L_s) coming from a direction of Ω' into the direction of Ω, r is the air-sea interface Fresnel reflectance corresponding to this mirror-reflection. If the skylight at the specular direction (L'_s) relative to Ω is measured [15] (Fig. 2), L_r can be estimated as:

$$L_r(\Omega) = \rho_s(\Omega) \times L'_s, \tag{3}$$

7

where

$$\rho_S(\Omega) = \frac{1}{L'_S} \int_{2\pi} p(\Omega' \to \Omega) \times r(\Omega' \to \Omega) \times L_s(\Omega')d\Omega'. \qquad (4)$$

ρ_s, the sea surface reflectance, is the ratio of the reflected skylight just above the water to the sky radiance measured at the specular direction. For a flat sea surface where we have only the mirror reflectance within the sensor FOV (weighted average of $L_s(\Omega')$ over the sensor FOV = L'_s), $p(\Omega' \to \Omega)$ becomes a Dirac delta function, and ρ_s simply would be equal to the Fresnel reflectance corresponding to this mirror-reflection. However, the field of view of some radiometers could be significant (~10°) therefore, measured radiance and skylight would be weighted averages over a range of viewing angles within the sensor FOV. In this case, ρ_s would be equal to an average of the Fresnel reflectance over the sensor field of view [4, 11].

Apparently, it is advantageous to use Eq. (3), as compared to Eq. (2), to estimate L_r because it only requires measurement of the skylight at the specular direction. However, it also requires knowledge of ρ_s [11]. ρ_s, as shown in Eq. (4), varies with observation angle and the distributions of both skylight and capillary wave facets.

ρ_s depends on p (sr^{-1}), the probability distribution function (PDF) of the capillary wave facets. We will discuss in detail that p varies with wind speed as well as direction [16, 17]. However, in many studies of sea surface reflectance [11, 15, 18-20] the effect of wind direction on ρ_s is not accounted for [4]. Therefore, the exact effect of wind directions on ρ_s and hence on above-water radiometry is still unknown which leads us to investigate the effect of wind directions on ρ_s.

Chapter II

Literature review

In Eq. (4) sea surface reflectance, ρ_s, is a function of the probability distribution function (PDF) of the capillary wave facets, p (sr^{-1}).

Probability distribution function of capillary wave facets

Cox and Munk Model, 1954;

To investigate the probability of sun-glint, Cox and Munk developed a statistical model regarding the probability distribution function of capillary wave facets on sea surface [16]. First of all, the geometry of reflectance of a point on the sea surface that gets reflected to the observer has been identified then the average of the brightness of such point in terms of frequency of occurrence investigated.

Regarding the geometry of reflectance, in Fig. 5, the coordinate system is centered at the sea surface where the y-axis is horizontally along the sun direction and the z-axis is upward along zenith. Assuming a capillary wave facet AB'C'D' is the tangent of the horizontal plane ABCD to the sea surface. The steepest ascent of the wave facet (AC') has a tilt angle of β with the ABCD plane and an azimuthal angle of α with the sun direction (y-axis) [16]. From Fig. 5:

$$n(\text{norm of the wave facet}) = (-\sin\alpha\sin\beta \ , \ -\cos\alpha\sin\beta \ , \ \cos\beta),$$

$$i(\text{incident ray}) = (0 \ , \ \text{-cos}\theta_i \ , \ -\sin\theta_i), \qquad (5)$$

$$r(\text{reflected ray}) = (\text{-}\sin\theta_r\sin\varphi_r \ , \ \text{-}\sin\theta_r\cos\varphi_r \ , \ \cos\theta_r).$$

According to the law of reflectance,

$$r - i = n.2\cos\omega. \qquad (6)$$
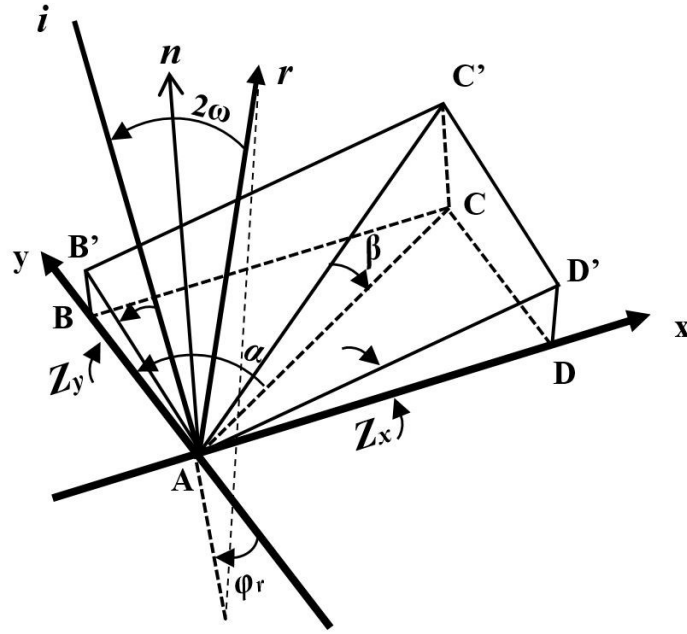
Figure 5. The geometry of reflectance of a capillary wave facet (AB'C'D') on the sea surface. i (incident ray) is coming from the sun and r (reflected ray) is pointed to the sensor where they make an angle of 2ω. n is the norm and β and α are required tilt and azimuth angles of the wave facet AB'C'D'.

From Eq. (5) and (6),

$$(-\sin\theta_r\sin\varphi_r, -\sin\theta_r\cos\varphi_r + \cos\theta_i, \cos\theta_r + \sin\theta_i) = (-2\cos\omega\sin\alpha\sin\beta, -2\cos\omega\cos\alpha\sin\beta, 2\cos\omega\cos\beta),$$
$$(7)$$

hence, the required orientation (β, α) of capillary wave facets for reflecting the incident ray to the direction of the reflected ray at point (A) would be:

10

$$\cos \beta = \frac{\cos \theta_r + \sin \theta_i}{2 \cos \omega}, \tag{8}$$

$$\cos \alpha = \frac{\sin \theta_r \cos \varphi_r - \cos \theta_i}{2 \cos \omega \sin \beta}, \tag{9}$$

where ω, the incident angle of the skylight at the reflection point (A) is:

$$\cos 2\omega = \cos \theta_i \cos \theta_r - \sin \theta_i \sin \theta_r \cos \varphi_r. \tag{10}$$

Additionally, from Fig. 5, we have Z (CC') along the steepest ascent of the wave facet equals to:

$$\begin{aligned} Z &= AC \times \tan \beta = \sqrt{(x^2 + y^2)} \times \tan \beta \\ Z_x &= \partial Z \big/ \partial x = \frac{2x}{2\sqrt{(x^2 + y^2)}} \times \tan \beta = \sin \alpha \tan \beta \\ \Rightarrow \quad Z_y &= \partial Z \big/ \partial y = \frac{2y}{2\sqrt{(x^2 + y^2)}} \times \tan \beta = \cos \alpha \tan \beta \end{aligned} \tag{11}$$

The Gaussian probability distribution function for two variables Z_x and Z_y is:

$$p = M \exp\{-\frac{1}{2}[\frac{1}{(1-\rho^2)\sigma_x^2}(Z_x - \bar{Z}_x)^2 + \frac{2\rho}{(1-\rho^2)\sigma_x\sigma_y}(Z_x - \bar{Z}_x)(Z_y - \bar{Z}_y) + \frac{1}{(1-\rho^2)\sigma_y^2}(Z_y - \bar{Z}_y)^2]\}, \tag{12}$$

where M is the constant of normalization and ρ is the correlation coefficient between Z_x and Z_y where Z_x and Z_y have zero mean values ($\bar{Z}_x = \bar{Z}_y = 0$). By a suitable rotation of the coordinate system, it is always possible to make $\rho = 0$. In the new x', y' coordinate system, the slope components $Z_{x'}$ and $Z_{y'}$ have standard deviations of $\sigma_{x'}$ and $\sigma_{y'}$, respectively. Hence, Eq. (12) becomes:

$$p = (2\pi\sigma_c\sigma_u)^{-1} \exp\{-\frac{1}{2}[(\frac{Z_{x'}}{\sigma_{x'}})^2 + (\frac{Z_{y'}}{\sigma_{y'}})^2]\} \tag{13}$$

In Cox and Munk [16, 17], the suitable rotation is the wind direction. From sun glitter photographs, they found p follows the bivariate normal distribution with the upwind (η) and crosswind (ξ) components of the slope of capillary wave facets (Fig. 6).

$$p_{\text{anisotropic}} = \left(\frac{1}{2\pi\sigma_c\sigma_u} \right) \exp\left(\frac{-\xi^2}{2\sigma_c^2} + \frac{-\eta^2}{2\sigma_u^2} \right). \tag{14}$$

$$\xi = \sin\alpha' \times \tan\beta; \eta = \cos\alpha' \times \tan\beta.$$

The two slope components are independent of each other and have standard deviations of σ_c and σ_u, respectively. In Fig. 6 and Eq. (14), α' and β represent the azimuth angle (relative to the wind direction) and the tilt angle of the norm (n) of the wave facet, respectively. Cox and Munk [16, 17] found that both σ_u and σ_c vary with the wind speeds (U) approximately linearly,

$$\sigma_u^2 = 0.00 + 3.16 \times 10^{-3} U \pm 0.004, \text{ and}$$
$$\sigma_c^2 = 0.003 + 1.92 \times 10^{-3} U \pm 0.002, \tag{15}$$

where the wind speed and direction were measured at 41 feet above the water level and $\pm$ values are the standard deviations of the observed values for σ_u and σ_c and the corresponding values computed from the linear approximation.
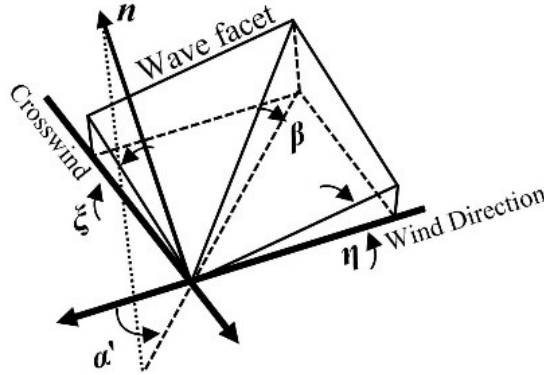
Figure 6. The geometric relationship between a capillary wave facet and wind direction. The coordinate system in Fig. 5 is rotated around the z-axis (zenith) where the new y-axis is along the wind direction. n is the norm and β and α are the required tilt and azimuth of wave facet. η is upwind and ξ is crosswind components of the slope of capillary wave facet.

Ignoring the effect of wind direction ($\sigma_u = \sigma_c$), we have an isotropic distribution where Eq. (14) becomes Eq. (16) [16, 17],

$$p_{\text{isotropic}} = \left(\frac{1}{\pi\sigma^2}\right)\exp\left(\frac{-\tan^2\beta}{\sigma^2}\right),\tag{16}$$

$$\sigma^2 = \sigma_c^{\,2} + \sigma_u^{\,2} = 0.003 + 5.12\times10^{-3}U \pm 0.004.\tag{17}$$

Wu Model, 1972;

Wu [21] found that the slope components vary with wind speeds non-linearly. Using the Cox and Munk measured mean-square slopes of the sea surface, Wu shows σ^2 increases less rapidly with the wind speed compared to the Cox and Munk linear model at lower wind speeds and more rapidly with higher wind speeds and they vary logarithmically with the wind speed (Eq. (18)).

$$\begin{aligned}\text{Wind speed} \leq 7; \sigma^2 &= (\ln U + 1.2)\times10^{-2}, \text{and}\\ \text{Wind speed} > 7; \sigma^2 &= (0.85\times\ln U - 1.45)\times10^{-1}.\end{aligned}\tag{18}$$

Mermelstein et al Model, 1994;

Mermelstein et al [22] suggested greater values for σ_u and σ_c than those used in Eq. (15) for wind speeds lower than 20 m s^{-1} (Eq. (19)). They integrated the wave height power spectral density (Fourier transform of correlation functions of the spatial and temporal wave height) with the Cox and Munk measured mean-square slopes of the sea surface and a non-linear relation was suggested for the σ_u and σ_c.

$$\begin{aligned}\sigma_u &= 0.091 + 0.019\times U - 4.6\times10^{-4}U^2, \text{and}\\ \sigma_c &= 0.059 + 0.021\times U - 5.5\times10^{-4}U^2.\end{aligned}\tag{19}$$

Shaw and Churnside Model, 1997;

To measure the glitter reflectance and the slope parameters in the Oregon coastal region, Shaw and Churnside [23] used a scanning-laser glint meter. They also suggested that the slope parameters would be related to the air-sea temperature difference if this difference meets a threshold. Shaw and Churnside's model is shown in Eqs. (20 and 21);

$$\sigma_u^2 = (0.000 + 3.16 \times 10^{-3} U) \times (1.42 - 2.8 Ri) \text{ , and}$$
$$\sigma_c^2 = (0.003 + 1.92 \times 10^{-3} U) \times (1.42 - 2.8 Ri), \tag{20}$$

when $-0.23 \leq Ri \leq 0.27$ and

$$\sigma_u^2 = (0.000 + 3.16 \times 10^{-3} U) \times 0.65 \text{ , and}$$
$$\sigma_c^2 = (0.003 + 1.92 \times 10^{-3} U) \times 0.65, \tag{21}$$

when $0.27 \leq Ri$. Ri is the reduced Richardson number and measured using Eq. (22).

$$Ri = g \frac{(T_a - T_w)}{T_w U^2} z, \tag{22}$$

where g (m s^{-2}) is gravitational acceleration, T_a and T_w are air and water temperature, respectively, and z is the wind speed measurement elevation from the top of the sea surface which in their model is 10 m.

Ebuchi and Kizu Model, 2002;

To measure the probability distribution of the capillary wave facets, Ebuchi and Kizu [24] used sun glitter images mostly taken at subtropical ocean area and found narrower standard deviations [25] of σ_c and σ_u compared to the Cox and Munk model;

$$\sigma_u^2 = 0.0053 + 6.71 \times 10^{-4} U, \text{and}$$

$$\sigma_c^2 = 0.0048 + 1.52 \times 10^{-3} U, \text{and} \tag{23}$$

$$\sigma^2 = 0.0101 + 2.19 \times 10^{-3} U.$$

Bréon and Henriot Model, 2006;

An effort to correct the Cox and Munk model is done by Bréon and Henriot [26]. Using (POLDER) Polarization and Directionality of the Earth's Reflectance data [27] and wind data from NASA, they found that the σ_c and σ_u are slightly different from the Cox and Munk model;

$$\sigma_u^2 = 0.001 + 3.16 \times 10^{-3} U, \text{and}$$

$$\sigma_c^2 = 0.003 + 1.85 \times 10^{-3} U. \tag{24}$$

Fig. 7 compares the standard deviations of the capillary wave facets calculated using different models as a function of the wind speed. The Mermelstein et al. show the largest and Ebuchi and Kizu the smallest standard deviations. Bréon and Henriot's model agrees well with the Cox and Munk model.
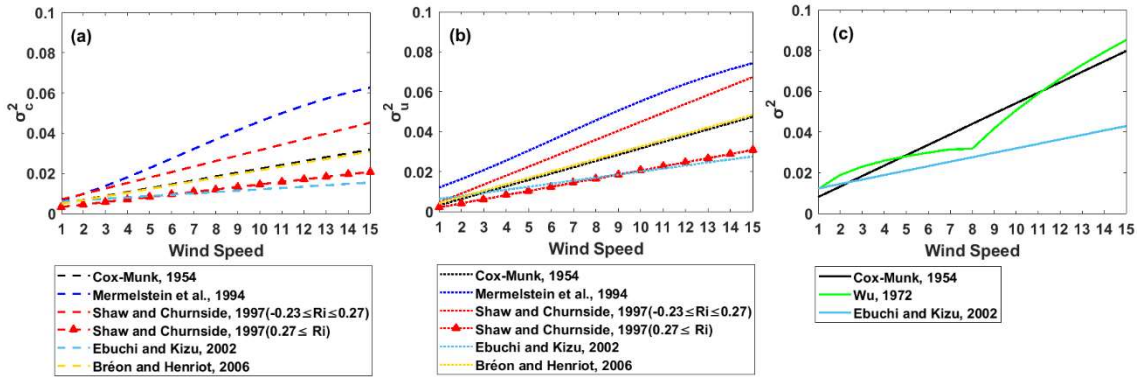
Figure 7. Standard deviations of the capillary wave facets for crosswind (a), upwind (b), and isotropic (c) are calculated using different models as a function of wind speed. For the Shaw and Churnside model, we assumed that T_a(air temperature) = T_w(water temperature) therefore, $Ri = 0$.

Zhang and Wang [25] reviewed these sea surface slope distribution models. They compared the sun glitter measurements from MODIS at 859 nm, 1240 nm, and 2130 nm with sun glitter modeled with these models and showed that the Cox and Munk, 1954 model (Eqs. (14 and 16)) mostly performs better than the other models in estimating the sun glint (Tables 1 and 2). Additionally, Fig. 6 in [25] shows that for the areas with smaller sun glint the anisotropic Cox and Munk model (Eq. (14)) performs slightly better than the isotropic model (Eq. (16)). Evaluation of these probability distribution functions of capillary wave facets models is of interest to this study. However, Cox and Munk's model is dominantly being used in the ocean optic studies. Therefore, we were convinced to use this model for this study.

Table 1: Linear fitting coefficients of sun glint models results for a MODIS image [25]. 1: Cox–Munk, 1954, isotropic; 2: Cox–Munk, 1954, anisotropic; 3: Ebuchi and Kizu, 2002, isotropic; 4: Ebuchi and Kizu, 2002, anisotropic; 5: Breon and Henriot, 2006, anisotropic; 6: Mermelstein et al., 1994, anisotropic; 7: Wu, 1972, isotropic.

Glint model	859 nm			1240 nm			2130 nm		
	correlation coefficient	Intercept $(*10^{-3})$	Slope	correlation coefficient	Intercept $(*10^{-3})$	Slope	correlation coefficient	Intercept $(*10^{-3})$	Slope
1	0.970	1.52	0.990	0.979	1.25	0.916	0.977	1.27	0.899
2	0.975	1.41	0.985	0.985	1.13	0.914	0.981	1.20	0.895
3	0.941	3.67	0.800	0.948	3.21	0.739	0.945	2.92	0.725
4	0.898	4.35	0.738	0.904	3.84	0.681	0.901	3.44	0.668
5	0.973	1.37	0.987	0.983	1.11	0.914	0.979	1.16	0.896
6	0.919	-1.46	1.360	0.931	-1.49	1.27	0.928	-1.00	1.24
7	0.943	3.02	0.831	0.951	2.61	0.738	0.948	2.42	0.754

Table 2: Correlation coefficient of sun glint models results at 2130 nm for 12 MODIS images [25]. The order of the models is the same as Table 1.

MODIS image	Model						
	1	2	3	4	5	6	7
1	0.965	0.966	0.946	0.931	0.969	0.916	0.945
2	0.979	0.985	0.948	0.904	0.983	0.931	0.951
3	0.965	0.962	0.941	0.934	0.96	0.92	0.945
4	0.981	0.986	0.951	0.921	0.986	0.94	0.959
5	0.97	0.977	0.929	0.898	0.978	0.946	0.934
6	0.973	0.975	0.956	0.927	0.975	0.935	0.971
7	0.982	0.984	0.964	0.945	0.983	0.941	0.969
8	0.986	0.987	0.956	0.944	0.987	0.942	0.974
9	0.973	0.985	0.935	0.872	0.985	0.935	0.957
10	0.969	0.97	0.961	0.952	0.97	0.941	0.973
11	0.981	0.982	0.955	0.933	0.983	0.937	0.973
12	0.958	0.957	0.926	0.914	0.956	0.94	0.952

Sea surface reflectance

Mueller and Austin, 1995;

Mueller and Austin [28] in ocean optics protocols for the SeaWiFS (Sea-Viewing Wide Field-of-View Sensor) validation assumed that the ρ_s is equal to Fresnel reflectance. However, as mentioned before, this assumption is valid only for a flat sea surface and ρ_s would be equal to the average of Fresnel reflectance over the sensor FOV [11].

Morel, 1980;

To estimate the ρ_s Morel [29] suggested measuring L_t (measured radiance) and L'_s (skylight) and assuming the L_w is equal to zero at the near-infrared (780 nm). Then apply a residual correction over the spectral L'_s to measure spectral correction of L_r (reflected skylight). However, he assumed that the ρ_s is spectrally flat. This approach is not practical for shallow or polluted waters where the water bed or sediments would scatter at the near-infrared range and $L_w = 0$ would not exist. Thereafter, Kutser et al. [30] suggested the same strategy but using two benchmarks spectrum at the farthest of both ultraviolet and near-infrared for coastal waters. They assumed that the water-leaving radiance is zero at 350–380 nm and 890–900 nm. In their study, a power function between these two benchmarks is suggested as spectral glint values.

Mobley, 1999;

Mobley [11] simulated ρ_s as a function of sun-sensor geometry and wind speeds. He divided the sky hemisphere to equal zenith and azimuth angles of 10° and 15° grids, respectively. Based on this partitioning, the solid angle for a grid centered at zenith angle 40° would be equal to 0.029 (sr) ($\Delta\cos\theta \times \Delta\varphi = (\cos35° - \cos45°) \times (15°\pi/180)$). This is almost equal to the corresponding circular sensor field of view (FOV) with half-angle of 5˚ ($2\pi(1-\cos5˚) =$

0.024) that measures the skylight at the viewing angle of 40°. Although these quads are quite large, he assumed the skylight is uniform within each quad. Random radiative rays were simulated within the grid at zenith angle 40° using Monte Carlo simulation [2]. He shows the rays were reflected from the sea surface centers the specular direction of the sensor and spreads around this point [11]. The sea surface was modeled using the isotropic Cox and Munk model [16, 17]. This simulation suggests $\rho_s \approx 0.028$ for $U \leq 5$ m s^{-1} and sensor viewing angle and azimuth angle of 40° and 45°, respectively. He shows that ρ_s increases with decreasing solar zenith angle and increases with increasing wind speeds. Additionally, he suggests a higher ρ_s for sensor azimuth angle of 90° [11]. Mobley assumed that ρ_s is independent of the wavelength because he assumed the same color for the entire skylight radiance (L_s) and the water refractive index (n) is spectrally flat. Additionally, both Mobley [31] and Harmel et al. [32] studied the impact of the skylight polarization on ρ_s. However, the spectral variation of ρ_s was not considered in their studies.

Lee et al. 2010;

When the sea surface is roughed due to U ≠ 0, the skylight contribution would come from different parts of the sky [11]. Therefore, there is a chance that light from the horizon or sun gets reflected to the sensor FOV, and the same color assumption for the entire skylight will be incorrect. Using a hyperspectral sensor and field measurement Lee et al. [33] show that ρ_s not only varies with sun-sensor geometry and wind speeds but in some cases, it changes by a factor of 8 from 400 nm to 800 nm. Briefly, from Eq. (1) and (3):

$$L_t = L_w + \rho_s L'_s,$$

(25)

where L'_s is skylight from the specular point of the sensor, thus:

$$\rho_s = \frac{L_t - L_w}{L'_s}$$

(26)

The spectral composition of the skylight from different directions is different. For example, it is more reddish around the sun and more white at the horizon at noon. Therefore, ρ_s will be spectrally dependent [33]. In their study, a hyperspectral sensor setup was used to measure the spectral variation of ρ_s, and in Eq. (26) parameters were replaced by reflectance:

$$\rho_s = \frac{T_{rs} - R_{rs}}{S_{rs}}$$

(27)

where T_{rs} (total remote sensing reflectance) is equal to L_t/E_d (E_d is downwelling irradiance), R_{rs} is remote sensing reflectance of water were estimated indirectly using the Morel and Maritorena [38] model, and S_{rs} is equal to L_{sky}/E_d [33].

To determine the downwelling irradiance (E_d), a standard diffuse reflector was used and assumed as a Lambertian reflection. in this case:

$$E_d = \frac{\pi L_G}{R_G},$$

(28)

where L_G is radiance reflected from standard diffuse reflector and R_G is the reflectance of the diffuse reflector [33].

Finally, to estimate the ρ_s using Eq. (27), T_{rs} and S_{rs} measured directly in the field using the hyperspectral sensor with a range of 360 nm to 900 nm and 2 nm resolution. To evaluate the estimated ρ_s, L_w was directly measured using a sensor where skylight was blocked using a black tube [34] and indirectly measured using Eq. (26). This study showed that the ρ_s is not spectrally independent especially for roughed sea surface which Mobly [11] ignored it before.

Zhang et al. 2017;

Zhang et al. [15] further investigated the spectral variation of ρ_s due to the skylight distribution and polarization as well. They simulated spectral variation of ρ_s as a function of sun-sensor geometry, wind speeds, and aerosol concentration [15]. Following Mobley [11] they partition the skydome into quads which instead of equal angular spacing, the quads have equal area subtend the exactly same solid angle as the sun ($\Omega_s = 6.8096 \times 10^{-5}$ sr) [15] but the shape for the sunlight would be a cone. This partitioning is important for two reasons. First, the skylight reflectance from the quads has equal weight and it only depends on sea state. Second, it allows separating the glints due to direct sunlight and diffuse skylight [15]. In this case,

$$\rho_S = \rho_{\text{Sun}} + \rho_{\text{Sky}}. \tag{29}$$

Like Mobley, the spatial distribution of probability (p) in this study (Fig. 2. in [15]) which the wind direction was ignored shows the skylight around the specular point of the sensor has the highest chance to get reflected to the sensor Field of View (FOV). Also, the probability of the skylight from directions away from the specular point of the sensor increases with wind speeds. They also investigated the spectral sea surface reflectance for sunlight and skylight separately by considering the spectral variation of the skylight and refractive index of water.

Zhang et al. [15] show the separated skylight reflectance, ρ_{sky}, increases with increasing the wind speed and increases with decreasing solar zenith angle. For a flat sea surface where ρ_{sky} would be equal to the average of Fresnel reflectance of the sensor FOV, they show that ρ_{sky} is more bluish since the refractive index of water and as a result, the Fresnel reflectance decreases toward the larger wavelengths. They show that for a windy sea surface (wind speed ≥ 5), the spectral ρ_{sky} increases toward the longer wavelengths because the skylight from the other directions than the specular direction of the sensor FOV is richer in the longer wavelengths (Fig. 5 in [15]).

For separated sunlight reflectance, ρ_{Sun}, they show that it increases with increasing the wind speed. ρ_{Sun} is more than 10% of ρ_{sky} when the sun is close to zenith ($\theta_{Sun} < 20°$) and the sea surface is moderate to highly roughed ($U > 10$ m s^{-1}) [15]. They show that ρ_{sun} is always reddish because the direct sunlight is much larger than the skylight from the specular direction of the sensor and it is less scattered at the larger wavelengths due to the Rayleigh scattering (Fig. 6 in [15]).

Zhang et al. [15] show that the total ρ_s ($\rho_{sun} + \rho_{sun}$) increases with increasing the wind speed and decreases with increasing the solar zenith angle. They show that in the cases where $\theta_{sun} < 20°$ and the wind speed > 10 m s^{-1}, total ρ_s increases more dramatically through the longer wavelengths. In the cases where ρ_{sun} is negligible, the total ρ_s shows the minimal spectral change and is smaller than 0.04 (Fig. 6 and 7 in [15]).

They found that ignoring the impact of polarization of skylight would cause underestimating the $\rho_{sky}(\lambda)$. In general, the spectral impact of polarization is opposite with the spectral skylight reflectance which shows a descending pattern towards longer wavelengths. They found that the polarization impact decreases with increasing the wind speed due to the depolarization of skylight by a highly roughed sea surface (Fig. 10 in [15]).

In these studies and many others on the skylight reflectance [11, 15, 18, 19, 33, 35-38] the wind direction was ignored [4] which led us to this research. In this study, we will compare the isotropic and the anisotropic Cox and Munk models to investigate the impact of wind direction on the sea surface reflectance.

Chapter III

Methodology

In this study, we followed the same approach used in Zhang et al. [15] except by additionally considering the wind directions in simulating the skylight reflectance. The polar coordinate system is presented in Fig. 8 where the sun is in the x-z plane. We partition the skydome into quads, each of which subtends the exactly same solid angle as the sun.
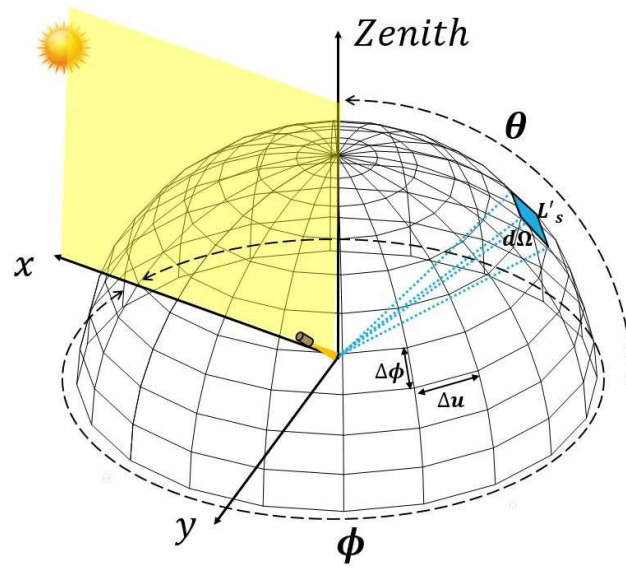
Figure 8. Schematic of the skydome partitioning. The coordinate system is defined by the sun in the x-z plane. $d\Omega = \Delta\phi \times \Delta u$ $(u = \cos\theta) = 6.8096 \times 10^{-5}$ [15]

As illustrated in Fig. 9, for a given configuration of a sensor (θ_{sensor}, φ_{sensor} representing zenith and azimuthal angles) and an arbitrary skydome quad (θ_{sky}, φ_{sky}), an orientation of capillary wave facets exists that would reflect the incoming skylight from this particular skydome quad into the sensor's field of view.

22
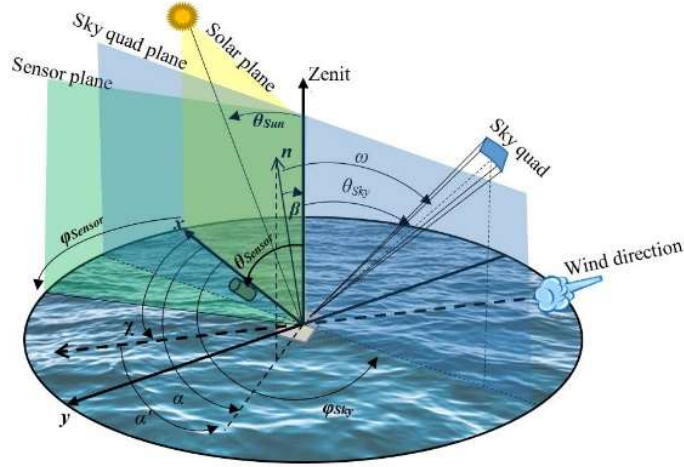
Figure 9. Schematic diagram showing the geometric relationship of an above-water radiometer that receives a surface-reflected skylight from an arbitrary direction by a randomly tilted capillary wave facet. The coordinate system is defined by the sun in the x-z plane, and the sloped facet placed in the origin. The polar coordinate (θ_{sky}, φ_{sky}) is for an arbitrary sky quad, (θ_{sensor}, φ_{sensor}) for the sensor, and (β, α) for the wave facet whose norm is defined as n.

The required orientation (β, α) of capillary wave facets from Eqs. 8 to 10 would be:

$$\cos\beta = \frac{\cos\theta_{sensor} + \cos\theta_{sky}}{2\cos\omega}, \tag{30}$$

$$\cos\alpha = \frac{\sin\theta_{sensor}\cos\varphi_{sensor} - \sin\theta_{sky}}{2\cos\omega\sin\beta}, \tag{31}$$

$$\cos 2\omega = \cos\theta_{sky}\cos\theta_{sensor} - \sin\theta_{sky}\sin\theta_{sensor}\cos\varphi_{sensor}. \tag{32}$$

To investigate the impact of the wind direction we simulated the sea surface using the Cox and Munk sea surface models. The probability of the wave facets is calculated as a function of the wind speed and ignoring the wind direction (isotropic Eq. (16)) and considering the wind direction (anisotropic Eq. (14)) in which $\alpha' = \alpha - \chi$ where χ is the wind direction relative to the sun (Fig. 9). To evaluate the impact of wind direction on sea surface reflectance we used the ratio of the anisotropic model to the isotropic model.

23

Apparently, the effect of the wind direction depends on the exact directional value of the wind relative to the sun and the sensor. As shown in Eq. (14), the wind directions only influence the $\frac{-\xi^2}{2\sigma_u^2} + \frac{-\eta^2}{2\sigma_c^2}$ term of the probability distribution function of capillary wave facets. A simple algebraic operation,

$$p_{aniso} = \left(\frac{1}{2\pi\sigma_c\sigma_u}\right)\exp\left(\frac{-\xi^2}{2\sigma_u^2} + \frac{-\eta^2}{2\sigma_c^2}\right) = A\times\exp\left(B\sin^2\alpha' + C\cos^2\alpha'\right)$$

$$\frac{d(p_{aniso})}{d\alpha'} = (\sin\alpha'\times\cos\alpha')\times A\times(2B - 2C)\times\exp\left(B\sin^2\alpha' + C\cos^2\alpha'\right)$$

(33)

shows that p_{aniso} reaches to maximum or minimum when $(\sin\alpha'\times\cos\alpha') = 0$, i.e. $\alpha' = 0°$ or $90°$, where α' ($\alpha' = \alpha - \chi$) represents the wind direction relative to the wave facet that would reflect the incoming skylight into the sensor. The probability reaches the maximum when the wind blows in a direction (χ) aligning with α (azimuthal angle of the capillary wave facet) and reaches a minimum with a perpendicular direction relative to α. For example, for $\theta_i = 0°$, and $\theta_r = 40°$, $\varphi_i = 45°$, we have $\alpha = 45°$ following Eqs. (30 to 32). It means the wind blowing in the same direction as the sensor (i.e., $\chi = 45°$) has the highest probability to produce a sun glint while the lowest probability at $\chi = 135°$ is expected. As the solar zenith angle increases the wind direction somewhere between the sun and the sensor would have the highest probability to produce a sun glint. For example, for $\theta_{Sun} = 40°$ and the same sensor setup ($\theta_{sensor} = 40°$, $\varphi_{sensor} = 45°$), we have $\alpha = 23°$ following Eqs. (30 to 32). This indicates that a wind blowing at $\chi = 23°$ produces the highest probability for seeing sun glint and the lowest probability at $\chi = 113°$. Table 3 shows an example of the wind directions representing the maximum and minimum of the anisotropic model for the sensor setup ($\theta_{sensor} = 40°$, $\varphi_{sensor} = 45°$):

Table 3. The wind directions in which the maximum and minimum of the anisotropic model were expected. Angles are counterclockwise from sun direction. (θ_{sensor}=40°, φ_{sensor}=45°)

Solar Zenith Angle	Wind direction for Maximum ρ_s	Wind direction for Minimum ρ_s
0°	45° (Sensor direction)	135° (Perpendicular to the Sensor direction)
10°	35°	125°
20°	30°	120°
30°	25°	115°
40°	23°	113°
50°	20°	110°
60°	19°	109°

In Eq. (4), the Quan and Fry 1995 equation [39] for the seawater refraction index is used to estimating the Fresnel reflectance (Eq. (34)). L_s (the skylight radiance) coming from an arbitrary direction is simulated using MODTRAN [40, 41] at different solar zenith angles and aerosol optical depth of 0.1 at 550 nm [15].

$$r(Fresnel\ reflectance) = \frac{1}{2}\left(\frac{\sin^2(\omega - \omega')}{\sin^2(\omega + \omega')} + \frac{\tan^2(\omega - \omega')}{\tan^2(\omega + \omega')} \right), \sin\omega' = \frac{1}{n}\sin\omega \tag{34}$$

$$n(S,T,\lambda)(refraction\ index) = n_0 + (n_1 + n_2T + n_3T^2)S + n_4T^2 +$$

$$\frac{n_5 + n_6S + n_7T}{\lambda} + \frac{n_8}{\lambda^2} + \frac{n_9}{\lambda^3}$$

$$T = Tempreture(°C), S = Salinity(\%), \lambda = Wavelength$$

where

$n_0 = 1.31405,\quad n_1 = 1.779\times10^{-4},\quad n_2 = -1.05\times10^{-6},$

$n_3 = 1.6,\times10^{-8}\quad n_4 = -2.02\times10^{-6},\quad n_5 = 15.868,$

$n_6 = 0.01155\quad n_7 = -0.00423,\quad n_8 = -4382,\quad n_9 = 1.1455\times10^6.$

As the Cox and Munk model has an inherent uncertainty relating the distribution of capillary wave facets to the wind speeds (Eqs. (14 and 16)), we estimated how this uncertainty would affect the sea surface reflectance to establish an uncertainty baseline. We varied the value of σ^2 computed by Eq. (16) within a range of $\pm$ 0.004 and the surface reflectance is simulated for various sun-sensor geometry and wind speeds (Fig. 10).
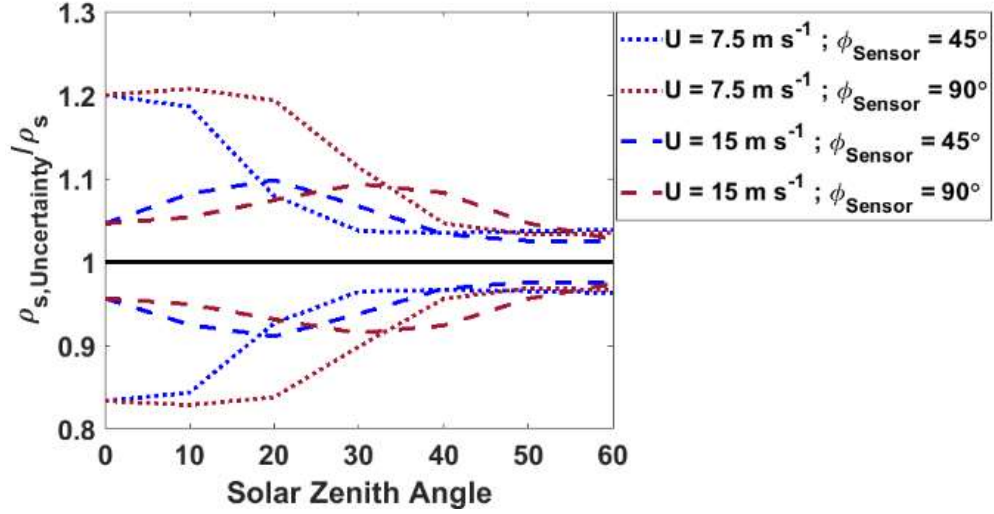
Figure 10. Ratios of ρ_s simulated assuming zero uncertainty in Eq. (16) to ρ_s simulated assuming an uncertainty of ±0.004 for various sun-sensor geometry and wind speeds with a fixed sensor zenith angle of 40°.

The effect of this inherent uncertainty on the reflectance depends strongly on solar zenith angle (θ_{Sun}) and wind speeds (U), reaching 20% for $\theta_{Sun} < 10°$ and $U < 7.5$ m s^{-1} and decreasing to $< 10\%$ for $\theta_{Sun} > 30°$ or $U > 10$ m s^{-1}. To a lesser degree, the effect also depends on the sensor's viewing geometry. For $\theta_{Sun} > 50°$, the effect is $< 5\%$ regardless of viewing geometry or wind speeds.

Now that we have established the baseline, inherent uncertainty on simulating the surface reflectance, we examine the effect of the wind direction. In particular, we followed Zhang et al. 2017 [15] to examine skylight glint ρ_{sky} and sun glint ρ_{Sun} separately where the PDF in Zhang et al. 2017 [15] model were replaced by Eqs. (14 and 16).

Chapter IV

Results

For a typical sensor setup, $\theta_{sensor} = 40°$ and $\varphi_{sensor} = 45°$, Fig. 11 shows the area of the skydome that would be seen by the sensor FOV for different wind speeds at 0, 7, and 15 m s^{-1}. As Fig. 2 in [15], this figure shows the reflected skylight area over the skydome increases with the wind speed. The highest probability for a sloped facet to reflect the skylight to the sensor FOV belongs to the quads around the specular point of the sensor (x). The probability decreases toward the opposite viewing directions where the lowest probability occurs for the quads near the horizon behind the sensor.
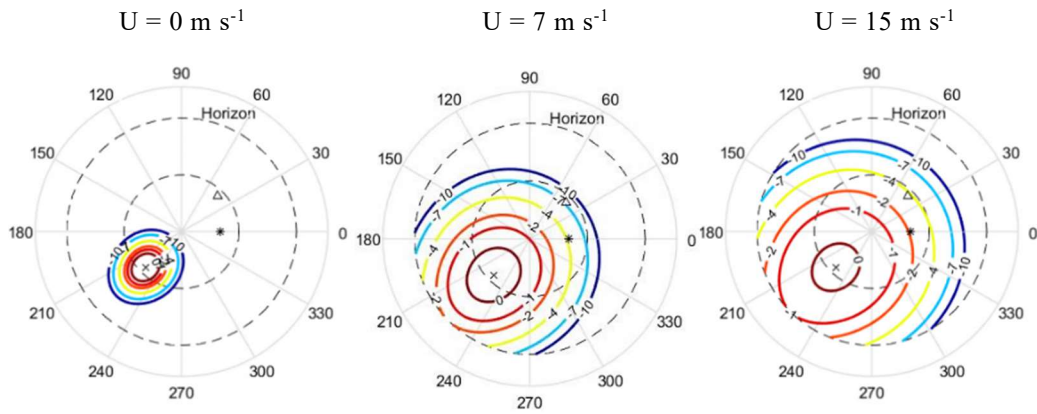
Figure 11. Contour plot of logarithmic isotropic p (sr^{-1}) as a function of skylight direction (θ, φ). The centers in each plot are the FOV of the sensor where θ is from 0° to 90° in radial direction and φ is azimuth angle from 0° to 360° counterclockwise relative to the sun. The *, Δ, and x symbols are sun at ($\theta_{sun} = 30°$, $\varphi_{sun} = 0°$), the sensor ($\theta_{ssensor} = 40°$, $\varphi_{sensor} = 45°$), and the specular point of the sensor ($\theta'_{sensor} = 40°$, $\varphi'_{sensor} = 225°$), respectively.

In the next step and to investigate the impact of the wind direction we simulated the PDF using Eq. (14). The logarithmic p (sr^{-1}) for different wind directions and cross-sections at different directions are shown in Fig. 12.
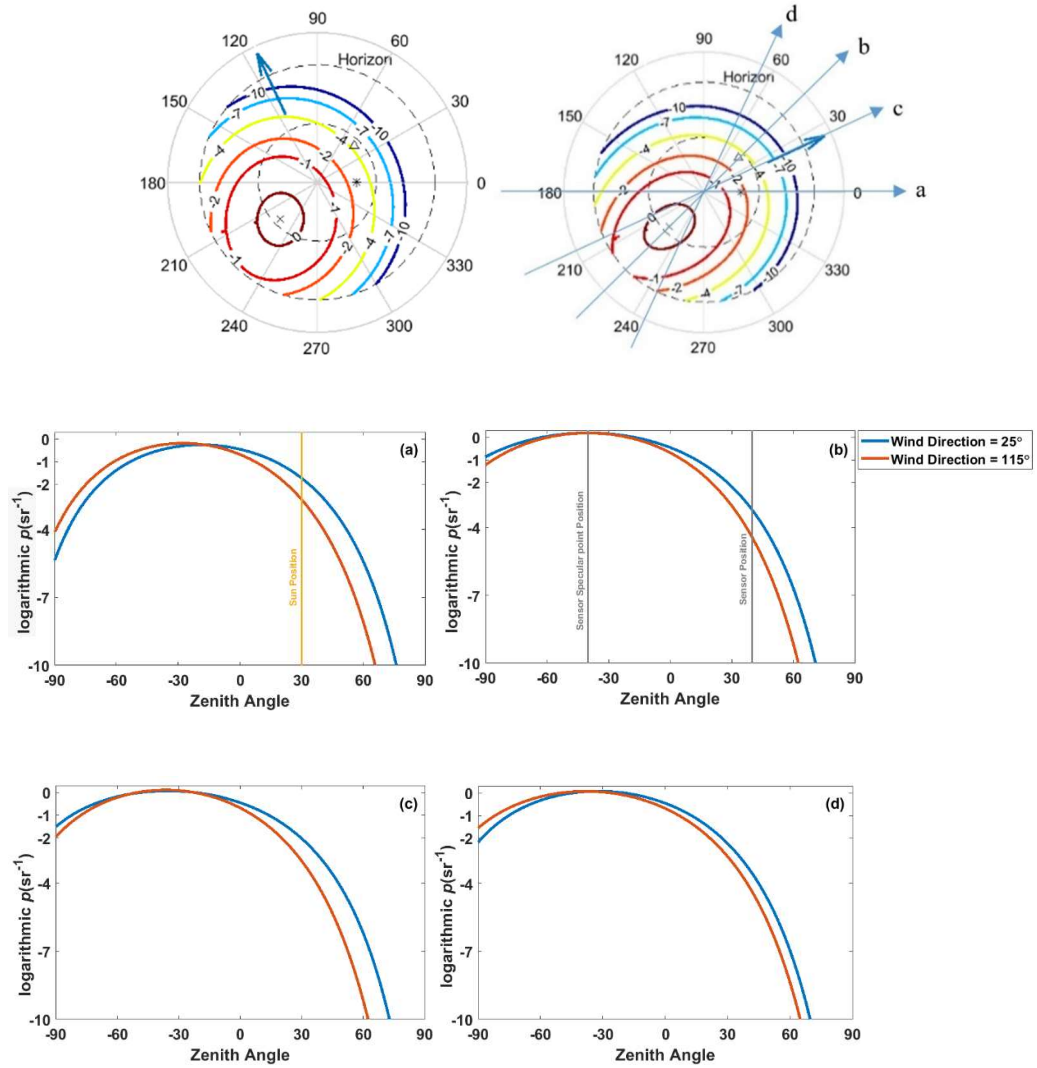
Figure 12. Contour plot of logarithmic anisotropic p (sr^{-1}) as a function of skylight direction (θ, φ) for wind speed = 15 m s^{-1} and the cross-sections along with the sun direction (a), the direction of 25˚ (b), the sensor direction (c), and the direction of 65˚ (d). The polar axes and symbols are the same as Fig. 11. The blue arrows are the wind directions and negatives in (a-d) means the specular directions.

Fig. 12(a) shows the probability for the slope facet at wind speed = 15 m s^{-1} to reflect the direct sun-beam, e.g. θ_{Sun} = 30°, when the wind blows at 25° degree counterclockwise from the sun direction is significantly higher than when the wind blows at 115° from ~1.6×10^{-2} (sr^{-1}) for χ = 25° to ~2×10^{-3}(sr^{-1}) for χ = 115°. It means a significant impact of the wind direction for the sunlight reflectance could be anticipated. The skylight reflectance is an integral over the entire sky dome (except the Sun disc). The cross-sections in Fig. 12 (a-d) show that at different wind directions (25° and 115°), although the probability for skylights increases in some portions of the sky, it decreases in the other portions. Hence it could be anticipated that the total skylight should not change significantly with the wind direction. To estimate the exact impact of the wind direction we simulate both sunlight and skylight reflectance as a function of wind direction. For the same sensor setup, the glint due to the direct sunlight is simulated as a function of wind direction and solar zenith angles. The ratios of the simulated ρ_{sun} using the anisotropic model (Eq. (14)) to the simulated ρ_{sun} using the isotropic model (Eq. (16)) is shown in Fig. 13. This figure shows that the effect of the wind direction on the sun glint can reach up to a factor of 10 either greater or smaller than the simulated reflectance with the isotropic model.

Figure 13. Ratios of the simulated ρ using the anisotropic model (Eq. 14) to the simulated ρ using the isotropic model (Eq. 16) for ρ_{sun} as a function of wind directions and solar zenith angles for a fixed sensor set up (θ_{sensor}=40°, φ_{sensor}=45°). Various lines in red color represent the inherent uncertainty in modeling the reflectance from Fig. 10.

As we explained in the methodology, in Fig. 13, it seems the wind directions somewhere between the sensor and the sun or perpendicular to these directions always show the highest impact of ignoring the wind direction where the maximum or minimum probability was expected (see the blue curves in Fig. 13).

For other solar zenith angles and sensor azimuth angles, the direct sunlight is simulated as a function of wind direction to estimate the maximum ρ_{sun} (Fig. 14). Fig. 14 shows that the impact of the wind direction on the sunlight reflectance is much larger than the inherent uncertainty in the modeling of the reflectance and it increases with increasing the solar zenith angle and decreasing the wind speed.

Figure 14. Absolute maximum ratios of the simulated ρ in Eq. (14) to the simulated ρ in Eq. (16) for ρ_{sun} as a function of solar zenith angles and sensor azimuth angles of 45°-90° for wind speeds of 7.5 and 15 m s^{-1}. Solid and dashed black lines are the uncertainties from Fig. 10.

Apparently, from Fig. 12(a) and 14, the impact of the wind direction regarding the solar zenith angle, to a lesser degree, is opposite to the probability for sensor seeing the direct sun-beam. For example in a highly roughed sea surface ($U = 15$ m s^{-1}), the probability decreases by

about two orders of magnitude from ~10^{-4} for $\theta_{Sun} = 40°$ to ~10^{-6} for $\theta_{sun} = 50°$ where the ratio of anisotropic to isotropic model only increases from ~3.5 to ~6.

Skylight reflectance is simulated as a function of the wind direction and the solar zenith angles. The ratios of the simulated ρ_{sky} using the anisotropic model (Eq. 14) to the simulated ρ_{sky} using the isotropic model (Eq. 16) is shown in Fig. 15. In contrast to the direct sunlight, the impact of the wind direction on skylight reflectance is negligible and the maximum impact is about 5% and it is almost always equal or smaller than the inherent uncertainty in the modeling of the reflectance.
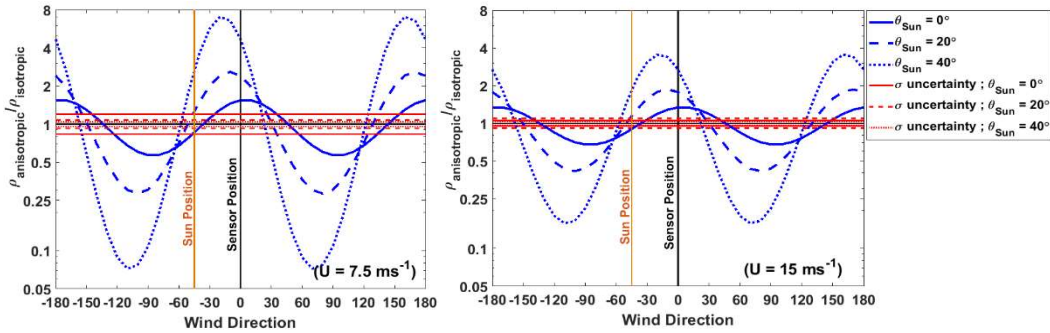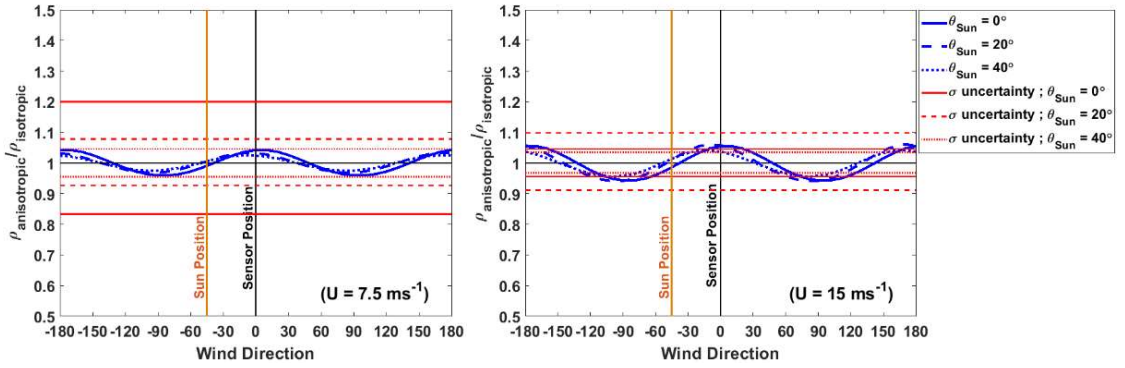

Figure 15. Ratios of the simulated ρ using the anisotropic model (Eq. 14) to the simulated ρ using the isotropic model (Eq. 16) for ρ_{sky} as a function of wind directions and solar zenith angles for a fixed sensor set up ($\theta_{sensor}=40°$, $\varphi_{sensor}=45°$). Various lines in red color represent the inherent uncertainty in the modeling of the reflectance.

From Fig. 13 and 15, it seems that the effect of the wind direction on skylight glint follows an approximately similar pattern as the sun glint because the skylight coming from the directions near the sun is the strongest, however, at a much-reduced intensity that is less than the inherent uncertainty.

For the other solar zenith angles and sensor azimuth angles, the skylight reflectance is simulated as the function of the wind direction to estimate the maximum ρ_{sky} (Fig. 16). This

31

figure shows the impact of the wind direction does not change significantly with the solar zenith angles, the sensor azimuth angle, or the wind speeds.
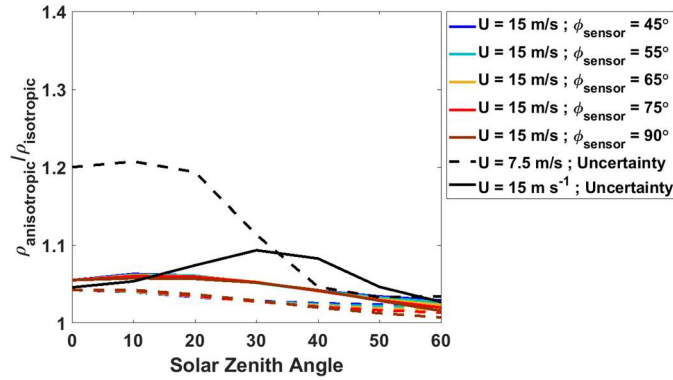
Figure 16. Absolute maximum ratios of the simulated ρ using Eq. (14) to the simulated ρ using Eq. (16) for ρ_{sky} as a function of solar zenith angles and sensor azimuth angles of 45°-90° and wind speeds of 7.5 and 15 ms^{-1}. Solid and dashed black lines are uncertainties from Fig. 10.

Combining the skylight reflectance and the glints due to the direct sunlight, the total impact of the wind direction on the ρ_s is >30% only when θ_{Sun} <20° or the wind speeds >12.5 ms^{-1} and θ_{Sun} < 40°. For the other environmental conditions when U < 7.5 m s^{-1} and θ_{sun} > 20°, the impact of the wind direction is generally less than or equal to the inherent uncertainty in the modeling of the reflectance and therefore can be ignored (Fig. 17).
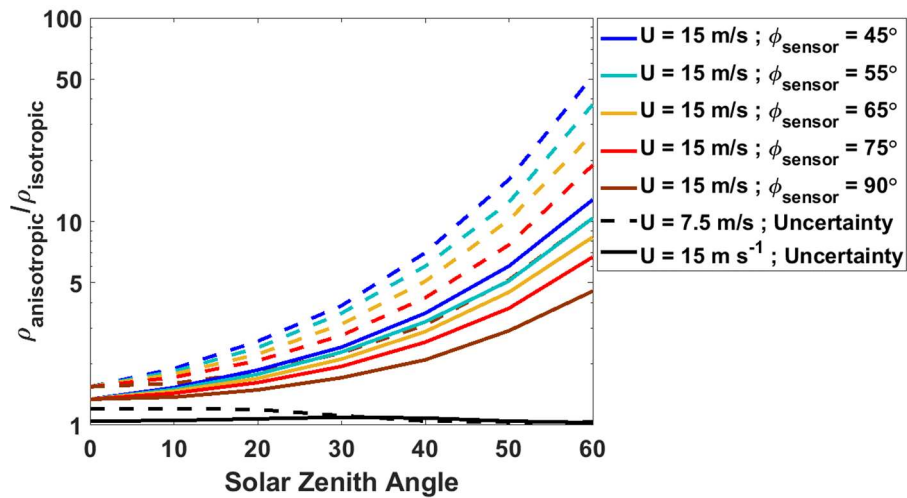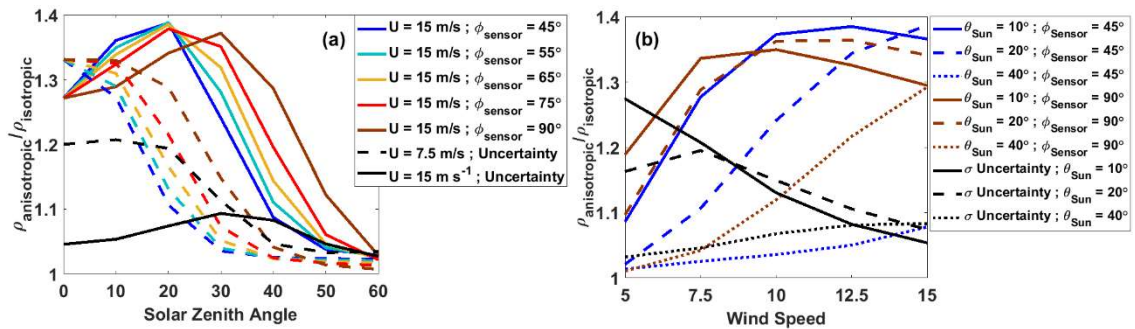

Figure 17. Absolute maximum ratios of the simulated ρ in Eq. (14) to the simulated ρ in Eq. (16) for ρ_s as a function of solar zenith angles for the sensor azimuth angles of 45°-90° (a) and wind speed (b). Solid and dashed black lines are uncertainties from Fig. 10.

From Fig. 17(a), apparently the senor azimuth angle of 90° (φ_{sensor} = 90°) is more sensitive to the wind direction where for a highly roughed sea surface (U = 15 m s^{-1}) or a moderate sea surface (U = 7.5 m s^{-1}) and θ_{sun} < 40° the impact of the wind direction is always greater than the inherent uncertainty.

From Fig. 17(b), it seems that for a highly roughed sea surface (U = 15 m s^{-1}) where the inherent uncertainty in the Cox and Munk model is less than 10%, the impact of the wind direction is up to 38%. This is shown that by increasing the wind speed, the impact of the wind direction becomes more significant compared to the inherent uncertainty.

To have a better view of the impact of the wind direction on skylight reflectance, we compared the simulated ρ_s using Zhang et al. [15], equivalent values extracted from tabulated data in Mobley [11], and the simulated ρ_s in our study using the anisotropic model for a typical sensor setup, where θ_{sensor} = 40°, and φ_{sensor} = 45° and U = 10 m s^{-1} (Fig. 18). This figure shows that ignoring the wind direction in Mobley and Zhang et al. models could exceed up to 39% and 31% underestimation or overestimation of ρ_s respectively for θ_{sun} = 10°.
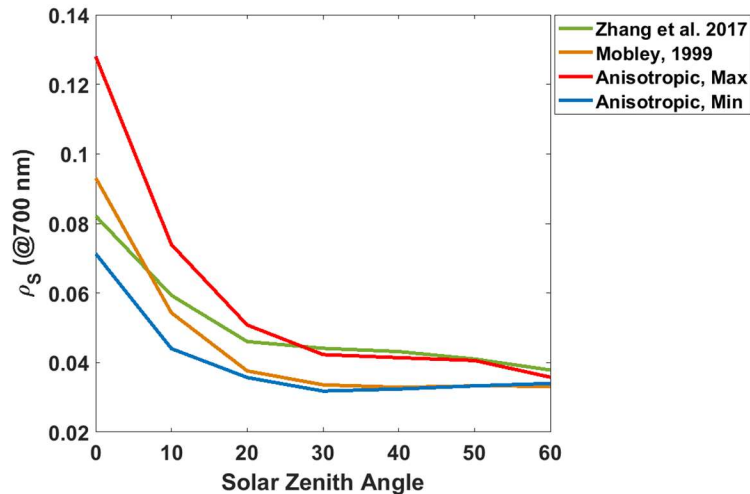
Figure 18. Maximum and minimum of the simulated ρ_s with Eq. (14) as a function of solar zenith angle where θ_{sensor} = 40° and φ_{sensor} = 45°, and U = 10 m s^{-1} compared to Zhang et al. 2017 at 700 nm and tabulated values from Mobley, 1999.

Chapter V

Discussion

Considering all sea surface models, the Cox and Munk model of the capillary wave facets is dominantly used for many instruments and sensors and it is shown that this model has better results in a wide range of conditions and sensors geometries [25, 42]. However, evaluating the other models is out of this paper's interest. Zhang and Wang [25] have shown in some cases (θ_{sensor}=35°, φ_{sensor}=140°, θ_{Sun}=20°, and U = 7.2 m s^{-1}) the isotropic Cox and Munk model shows about 20% smaller glitter radiance for the wind direction about 70° away from the sun in comparison to the anisotropic model. They show that with decreasing the angle between the wind direction and the sun, the anisotropic and the isotropic models show smaller glitter radiance difference. The ratio of the simulated ρ_{sun} using the anisotropic model (Eq. 14) to the simulated ρ_{sun} using the isotropic model (Eq. 16) for such sun-sensor setup and the wind speeds of 7 and 15 m s^{-1} is shown in Fig. 19 and the ratio of ~20% for the wind direction of 70˚ away from the sun is presented. However, our study covers the wind speeds higher than 7 m s^{-1} and the other wind directions are investigated, not only for the direct sun glint, also for the separated skylight and the total sea surface reflectance (sun and skylight glint).
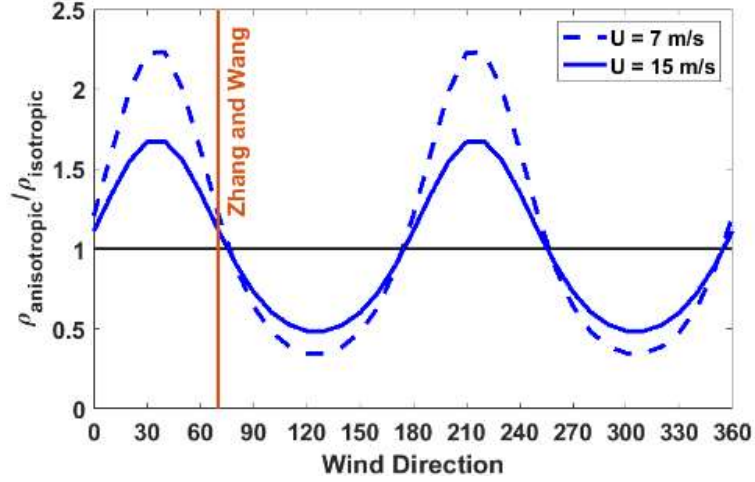
Figure 19. Ratios of the simulated ρ using the anisotropic model (Eq. 14) to simulated ρ using the isotropic model (Eq. 16) for ρ_{sun} where $\theta_{sensor}=35°$, $\varphi_{sensor}=140°$, $\theta_{Sun}=20$. The orange line is one example from Zhang and Wang [25].

The effect of polarization of the skylight has been simulated in some studies [15, 31, 32, 43] and is shown that for the low wind speeds or the large solar zenith angles the polarization of the skylight needs to be considered. Mobley and Zhang et al. [15, 31] show that the impact of the polarization of skylight for wind speed $= 10$ m s^{-1} and solar zenith angle $=$ 30˚ is almost 30% and in average is mostly larger than 10%. Mobley [31] investigated the polarized reflectance where the sea surface was formulated using the anisotropic wave variance spectra and Fast Fourier transforms ([31]). He only investigated the wind directions alongside and crossed the sun direction. He showed that the impact of wind direction on the polarized skylight reflectance becomes significant for the sensor viewing angles close to the nadir. Using polarized ray tracing, he showed that the winds blowing crossed the sun direction have larger ρ_s compared to the winds blowing along the sun direction due to the smaller wave slope variance (Fig. 18 in [31]). However, our study shows that the winds blowing somewhere between the sun and the sensor direction would show the maximum and perpendicular to this direction would show the minimum ρ_s. Similar to our result, Mobley [31] shows that the impact

35

of the wind direction increases with decreasing solar zenith angle due to the stronger skylight coming from the directions near the sun. Mobley and Zhang et al. [15, 31] show that the polarized skylight reflectance decreases with increasing the wind speed because the roughed sea surface depolarizes the skylight.

In Eq. (2), water temperature, salinity, wavelength, polarization, and aerosol optical depth only impact the r (air-sea interface Fresnel) and the L_S (Skylight). Because these parameters do not change with the wind speed or direction they are ignored in this study.

To decrease the uncertainties of the estimation of ρ_s, the viewing angle and azimuth angle of the sensor should be closely monitored. It has been shown that $\theta_{sensor} < 40°$ is mostly carrying sun glint [11] and $\theta_{sensor} > 40°$ is more sensitive to the small changes in the sensor viewing angles [36]. Additionally, it has been mentioned that the azimuth angle for the water measurement and the sky radiance measurement should be the same due to the significant distribution change of the skylight at the different azimuth angles [36].

Cloud coverage has not been taken to account in this study. However, clouds would impact the illumination especially near the sun, and it will impact the E_d and as a result every other related parameter. Mobley [11] has indicated the impact of the cloud coverage suggesting the value of $\rho_s \approx 0.028$ for the overcast sky. Cui et al. [37] investigated the spectral ρ_s for the overcast sky and suggested a flat spectral ρ_s from 400nm to 800 nm.

Chapter VI

Conclusions

Multiple studies have investigated the sea surface reflectance as a function of the geometry of the sensor-sun, wavelength, polarization, and the water surface roughness. Many models developed to post-process the observations. However, the estimation of skylight reflectance still carries many uncertainties.

This study has focused on the impact of the wind direction over the water surface state and the sea surface reflectance. For solar zenith angle $= 0°$, the maximum ρ_{sun} is where the wind blows along the sensor direction and the minimum is perpendicular to this direction. For solar zenith angle $\neq 0°$, the pattern is the same but in this case, the maximum of ρ_{sun} is when the wind blows between the sun and the sensor. The pattern for the maximum and the minimum of the ρ_{sky} as a function of wind direction is the same as ρ_{sun} which mostly comes from the skylight near the sun.

We showed that for a roughed sea surface (U=15 m s^{-1}) and sun close to the zenith, the difference between isotropic and anisotropic Cox and Munk model is very significant and much higher than the uncertainty of the estimation of σ. This is mostly because of the high direct sunlight reflectance and should not be ignored. In Fig. 18 we show that ignoring the wind direction in a moderate sea surface ($U > 10$ m s^{-1}) when the sun is close to the zenith ($\theta_{sun} < 10°$) could lead to >30% underestimation or overestimation of ρ_{s}.

In most of the above-water measurements, the sensor azimuth angle is set to larger than 40° away from the sun (45°-90°) to avoid the presence of the sun glint in the observations. We suggest the anisotropic sea surface reflectance model for a sensor setup near the equator that the presence of the sun glint is unavoidable around noon.

For the sensor azimuth angle of 45˚, the total impact of the wind direction on ρ_s when $U < 7.5$ m s^{-1} and $\theta_{sun} > 20°$ or $\theta_{Sun} > 40°$ with any wind speed is generally less than or equal to the inherent uncertainty of the Cox and Munk isotropic model and can be ignored (Fig. 20(a)). For the sensor azimuth angle of 90˚, the impact of the wind direction is mostly greater than the inherent uncertainty except for a very calm sea surface ($U < 5$ m s^{-1}) or $\theta_{sun} > 50°$ and wind speed < 12.5 m s^{-1} (Fig. 20(b)). The impact of the wind direction always is $> 20\%$ when $\theta_{sun} < 20°$ and $U > 5$ m s^{-1}. However, for $\varphi_{sensor} = 90°$, the impact of the wind direction for any solar zenith angles could reach to $> 20\%$ if $U > 12.5$ m s^{-1}.
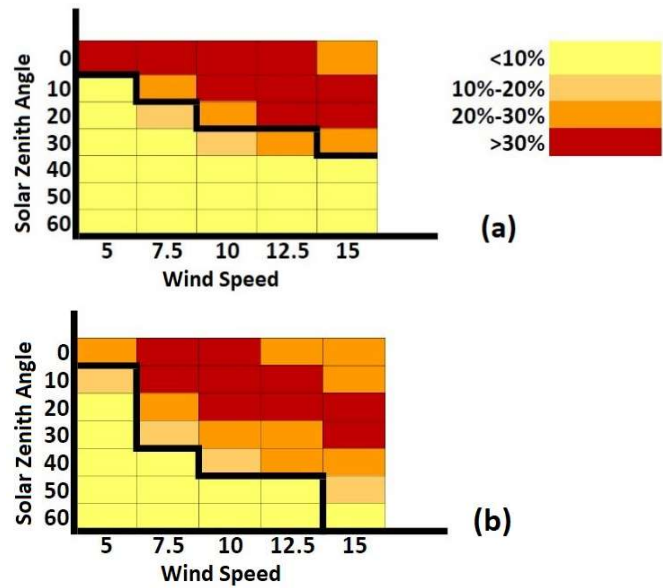
Figure 20. The maximum impact of the wind direction as a function of wind speed and the solar zenith angle for $\varphi_{sensor} = 45°$ (a) and $\varphi_{sensor} = 90°$ (b). The black line is the inherent uncertainty. The impact of the wind direction for blocks above this line are larger than the inherent uncertainty.

Table 4. Abbreviations and symbols

L_w	Water-leaving radiance
L_{wn}	Nadir water-leaving radiance
$L_{un(z)}$	Nadir upwelling radiances at different water depths (z)
L_t	Measured radiance by the sensor's field of view
L_r	Skylight reflected into the sensor's field of view
E_d	Downwelling irradiance
ρ	Correlation Coefficient
FOV	Field Of View
Ω	Solid angle
p (PDF)	Probability Distribution Function
L_s	Skylight
L'_s	Skylight from the specular direction of the sensor
r	Fresnel Reflectance
ρ_s	Total Skylight Reflectance
ρ_{sky}	Separated Skylight Reflectance
ρ_{sun}	Separated Sunlight Reflectance
ω	Incident angle of the skylight at the reflection point
n	Refractive index of air-sea water
ξ	Crosswind component of the slope of capillary wave facets
η	Upwind component of the slope of capillary wave facets
σ_c	Crosswind standard deviation of the slope of capillary wave facets
σ_u	Upwind standard deviation of the slope of capillary wave facets

σ	standard deviation of the slope of capillary wave facets (regardless of wind direction)
α	Azimuth angle (relative to the Sun direction) of the norm of the wave facet
α'	Azimuth angle (relative to the wind direction) of the norm of the wave facet
β	Tilt angle of the norm (n) of the wave facet
n	Norm of the wave facet
U	Wind speed
χ	Wind direction
λ	Wavelength
θ_{sun}	Solar zenith angle
θ_{sky}	Sky-partition zenith angle
φ_{sky}	Sky-partition azimuth angle
θ_{sensor}	Sensor viewing (zenith) angle
φ_{sensor}	Sensor azimuth angle
g	Gravitational acceleration
Ri	Reduced Richardson number
T_a	Air temperature
T_w	Water temperature
S	Salinity
T_{rs}	Total remote sensing reflectance
S_{rs}	Total skylight
E_d	Downwelling irradiance
R_{rs}	Remote sensing reflectance
L_G	Radiance reflected from the standard diffuse reflector
R_G	Reflectance of the diffuse reflector

References

1. Dierssen, H.M. and K. Randolph, *Remote Sensing of Ocean Color*, *In: Orcutt J. (eds) Earth System Monitoring.* Springer, 2013, p. 439-472.

2. Mobley, C.D., *Light and water: radiative transfer in natural waters*. Academic Press, 1994.

3. Platt, T., N. Hoepffner, V. Stuart, and C. Brown, *Why ocean colour? The societal benefits of ocean-colour technology*. International Ocean-Colour Coordinating Group, No. 7, 2008.

4. Ruddick, K.G., K. Voss, A.C. Banks, E. Boss, A. Castagna, R. Frouin, M. Hieronymi, C. Jamet, B.C. Johnson, and J. Kuusk, *A Review of Protocols for Fiducial Reference Measurements of WaterLeaving Radiance for Validation of Satellite Remote-Sensing Data over Water.* Remote Sensing, 2019, 11(19): p. 2198.

5. Clark, D.K., M.A. Yarbrough, M. Feinholz, S. Flora, W. Broenkow, Y.S. Kim, B.C. Johnson, S.W. Brown, M. Yuen, and J.L. Mueller, *MOBY, a radiometric buoy for performance monitoring and vicarious calibration of satellite ocean color sensors: Measurement and data analysis protocols. Chapter 2.* 2003.

6. Antoine, D., P. Guevel, J.-F. Desté, G. Bécu, F. Louis, A.J. Scott, and P. Bardey, *The "BOUSSOLE" buoy—A new transparent-to-swell taut mooring dedicated to marine optics: Design, tests, and performance at sea.* Journal of Atmospheric and Oceanic Technology, 2008, 25(6): p. 968-989.

7. Antoine, D., A. Morel, E. Leymarie, A. Houyou, B. Gentili, S. Victori, J.-P. Buis, N. Buis, S. Meunier, M. Canini, D. Crozel, B. Fougnie, and P. Henry, *Underwater Radiance Distributions Measured with Miniaturized Multispectral Radiance Cameras.* Journal of Atmospheric and Oceanic Technology, 2013, 30(1): p. 74-95.

8. Gordon, H.R. and K. Ding, *Self-shading of in-water optical instruments.* Limnology and Oceanography, 1992, 37(3): p. 491-500.

9. Leathers, R.A., T.V. Downes, and C.D. Mobley, *Self-shading correction for oceanographic upwelling radiometers.* Optics Express, 2004, 12(20): p. 4709-4718.

10. Zibordi, G. and G. Ferrari, *Instrument self-shading in underwater optical measurements: experimental data.* Applied Optics, 1995, 4(15): p. 2750-2754.

11. Mobley, C.D., *Estimation of the remote-sensing reflectance from above-surface measurements.* Applied Optics, 1999, 38(36): p. 7442-7455.

12. Garaba, S.Z.O., *Methods in reducing surface reflected glint for shipborne above-water remote sensing.* Journal of the European Optical Society-Rapid Publications, 2013, 8: p. 13058.

13. Lee, Z., N. Pahlevan, Y.-H. Ahn, S. Greb, and D. O'Donnell, *Robust approach to directly measuring water-leaving radiance in the field.* Applied Optics, 2013, 52(8): p. 1693-1701.

14. Tanaka, A., H. Sasaki, and J. Ishizaka, *Alternative measuring method for water-leaving radiance using a radiance sensor with a domed cover.* Optics Express, 2006, 14(8): p. 3099-3105.

15. Zhang, X., S. He, A. Shabani, P.-W. Zhai, and K. Du, *Spectral sea surface reflectance of skylight.* Optics Express, 2017, 25(4): p. A1-A13.

16. Cox, C. and W. Munk, *Measurement of the roughness of the sea surface from photographs of the sun's glitter.* Journal of the Optical Society of America, 1954, 44(11): p. 838-850.

17. Cox, C. and W. Munk, *Slopes of the sea surface deduced from photographs of sun glitter.* Scripps Digital Collection, 1956.

18. Gordon, H.R. and M. Wang, *Surface-roughness considerations for atmospheric correction of ocean color sensors. 1: The Rayleigh-scattering component.* Applied Optics, 1992, 31(21): p. 4247-4260.

19. Gordon, H.R. and M. Wang, *Retrieval of water-leaving radiance and aerosol optical thickness over the oceans with SeaWiFS: a preliminary algorithm.* Applied Optics, 1994, 33(3): p. 443-452.

20. Mueller, J.L., G.S. Fargion, C.R. McClain, S. Pegau, J.R.V. Zanefeld, B.G. Mitchell, M. Kahru, J. Wieland, and M. Stramska, *Ocean optics protocols for satellite ocean color sensor validation, revision 4, volume IV: Inherent optical properties: Instruments, characterizations, field measurements and data analysis protocols.* 2003.

21. Wu, J., *Sea-surface slope and equilibrium wind-wave spectra.* The Physics of Fluids, 1972, 15(5): p. 741-747.

22. Mermelstein, M.D., E.P. Shettle, E.H. Takken, and R.G. Priest, *Infrared radiance and solar glint at the ocean–sky horizon.* Applied Optics, 1994, 33(25): p. 6022-6034.

23. Shaw, J.A. and J.H. Churnside, *Scanning-laser glint measurements of sea-surface slope statistics.* Applied Optics, 1997, 36(18): p. 4202-4213.

24. Ebuchi, N. and S. Kizu, *Probability distribution of surface wave slope derived using sun glitter images from geostationary meteorological satellite and surface vector winds from scatterometers.* Journal of Oceanography, 2002, 58(3): p. 477-486.

25.   Zhang, H. and M. Wang, *Evaluation of sun glint models using MODIS measurements.* Journal of Quantitative Spectroscopy and Radiative Transfer, 2010, 111(3): p. 492-506.

26.   Bréon, F. and N. Henriot, *Spaceborne observations of ocean glint reflectance and modeling of wave slope distributions.* Journal of Geophysical Research: Oceans, 2006, 111(C6).

27.   Deschamps, P.-Y., F.-M. Bréon, M. Leroy, A. Podaire, A. Bricaud, J.-C. Buriez, and G. Seze, *The POLDER mission: Instrument characteristics and scientific objectives.* IEEE Transactions on Geoscience and Remote Sensing, 1994, 32(3): p. 598-615.

28.   Mueller, J.L. and R.W. Austin, *Ocean optics protocols for SeaWiFS validation, revision 1.* SeaWiFS Technical Report Series, Vol. 25, NASA Technical Memorandom 104566, 1995.

29.   Morel, A., *In-water and remote measurements of ocean color.* Boundary-layer Meteorology, 1980, 18(2): p. 177-201.

30.   Kutser, T., E. Vahtmäe, B. Paavel, and T. Kauer, *Removing glint effects from field radiometry data measured in optically complex coastal and inland waters.* Remote Sensing of Environment, 2013, 133: p. 85-89.

31.   Mobley, C.D., *Polarized reflectance and transmittance properties of windblown sea surfaces.* Applied Optics, 2015, 54(15): p. 4828-4849.

32.   Harmel, T., A. Gilerson, A. Tonizzo, J. Chowdhary, A. Weidemann, R. Arnone, and S. Ahmed, *Polarization impacts on the water-leaving radiance retrieval from above-water radiometric measurements.* Applied Optics, 2012, 51(35): p. 8324-8340.

33.   Lee, Z., Y.-H. Ahn, C. Mobley, and R. Arnone, *Removal of surface-reflected light for the measurement of remote-sensing reflectance from an above-surface platform.* Optics Express, 2010, 18(25): p. 26313-26324.

34.   Ahn, Y., J. Ryu, and J. Moon, *Development of redtide & water turbidity algorithms using ocean color satellite.* KORDI Report No. BSPE 98721–00–1224–01, 1999.

35.   Wang, M. and S.W. Bailey, *Correction of sun glint contamination on the SeaWiFS ocean and atmosphere products.* Applied Optics, 2001, 40(27): p. 4790-4798.

36.   Gilerson, A., C. Carrizo, R. Foster, and T. Harmel, *Variability of the reflectance coefficient of skylight from the ocean surface and its implications to ocean color.* Optics Express, 2018, 26(8): p. 9615-9633.

37.   Cui, T.-W., Q.-J. Song, J.-W. Tang, and J. Zhang, *Spectral variability of sea surface skylight reflectance and its effect on ocean color.* Optics Express, 2013, 21(21): p. 24929-24941.

38. Fougnie, B., R. Frouin, P. Lecomte, and P.-Y. Deschamps, *Reduction of skylight reflection effects in the above-water measurement of diffuse marine reflectance.* Applied Optics, 1999, 38(18): p. 3844-3856.

39. Quan, X. and E.S. Fry, *Empirical equation for the index of refraction of seawater.* Applied Optics, 1995, 34(18): p. 3477-3480.

40. Berk, A., G. Anderson, P. Acharya, L. Bernstein, L. Muratov, J. Lee, M. Fox, S. Adler-Golden, J. Chetwynd, M. Hoke, R. Lockwood, J. Gardner, T. Cooley, C. Borel, P. Lewis and E. Shettle. *MODTRAN5: 2006 update.* Algorithms and Technologies for Multispectral, Hyperspectral, and Ultraspectral Imagery XII, 2006, p. 62331F.

41. Doerffer, R., H. Schiller, J. Fischer, R. Preusker, and M. Bouvet. *The impact of sun glint on the retrieval of water parameters and possibilities for the correction of MERIS scenes*. In Proceedings of the 2nd MERIS-(A)ATSR Workshop, 2008.

42. Kay, S., J.D. Hedley, and S. Lavender, *Sun glint correction of high and low spatial resolution images of aquatic scenes: a review of methods for visible and near-infrared wavelengths.* Remote Sensing, 2009, 1(4): p. 697-730.

43. Zhai, P.-W., Y. Hu, J. Chowdhary, C.R. Trepte, P.L. Lucker, and D.B. Josset, *A vector radiative transfer model for coupled atmosphere and ocean systems with a rough interface.* Journal of Quantitative Spectroscopy and Radiative Transfer, 2010, 111(7-8): p. 1025-1040.